Interaction between Instabilities in Vertical Axis Turbine Blades

Benjamin Terry

A thesis
submitted in partial fulfillment of the
requirements for the degree of

Master of Science

University of Washington

2022

Committee:

Richard Wiebe

Michael Motley

Travis Thonstad

Paolo Calvi

Program Authorized to Offer Degree:
Civil and Environmental Engineering

University of Washington

Abstract

Interaction between Instabilities in Vertical Axis Turbine Blades

Benjamin Terry

Chair of the Supervisory Committee:
Richard Wiebe
Department of Civil and Environmental Engineering

This work investigates five different instability mechanisms which may occur in straight-bladed H-rotor vertical axis turbines. Specifically, it considers the static instabilities of divergence and centrifugal buckling as well as the dynamic instabilities of flutter, main resonance, and parametric resonance. This is done by applying Theodorsen's model for unsteady aerodynamics with traditional finite element methods. The resulting model is comprised of bend-twist-coupled elements which inherently account for fluid and centrifugal effects. A validation study is conducted to assess the accuracy and limitations of the model using experimental data from the existing literature. Eigenvalue analysis is used on time-averaged equations to predict divergence, flutter, and centrifugal buckling, as well as identify regions where main and parametric resonance could be excited. Time history analysis is then used to confirm these predictions and show main and parametric resonance explicitly. Results show good agreement in the prediction of centrifugal buckling and main and parametric resonances excited with respect to twisting. Neither type of resonance is observed with respect to bending. Flutter is predicted to occur via eigenvalue analysis but is not observed via time history analysis due to the limited applicability of Theodorsen's model in the time-domain. A discrepancy with the divergence boundary is also observed due to an unexpected region of "parametric stabilization" which is found to extend into regions predominated by static instability.

TABLE OF CONTENTS

LIST OF FIGURES

LIST OF TABLES

ACKNOWLEDGMENTS

I would like to take this opportunity to thank my family for their continual love and support. Each of you has had a tremendous impact on the person I am today, and I could never have gotten this far without you.

I would also like to express my gratitude to my research advisors, Dr. Richard Wiebe and Dr. Mike Motley, for guiding my curiosity and fostering my exploration of the wide world of academia. I will always value this time I got to spend among the ranks of some truly world-class academics.

I would also like to thank my academic advisor, Dr. Travis Thonstad, for helping me navigate my first few quarters of graduate school, helping me find this amazing research project, and for agreeing to be on my thesis defense committee. The conversations we had were instrumental in helping me figure out my path.

Thank you to Dr. Paolo Calvi for also agreeing to be on my thesis defense committee and for giving me a solid foundation in structural dynamics. This paper would not have been possible without the things you taught me.

Thank you to Dr. John Stanton for igniting my passion for all things structural. And thank you to Sam Turner, Stephan Ahn, and Danielle Voytko for offering me my first unfiltered glimpses into the ups and downs of graduate school when I was an undergraduate research assistant.

This work was supported by the US Department of Energy through Grant # DE-AR0001441. 2D CFD data provided by the University of Wisconsin-Madison, Department of Engineering Physics.

Chapter 1
INTRODUCTION

1.1 Background

Wind- and water-powered turbines are continuing to become more popular as the world shifts towards renewable sources of energy. As this technology continues to develop and the scale of these turbines increase, concerns about their structural stability have become more relevant.

Turbines generally fall into one of two categories. Horizontal Axis Turbines (HATs) are those which have incoming flow parallel to the turbine's axis of rotation. Wind-powered HATs are commonly used in offshore regions where a single turbine can generate power in the megawatt range [4]. Vertical Axis Turbines (VATs), also known as cross-flow turbines, are those which have incoming flow perpendicular to the turbine's axis of rotation. These turbines are deployed in regions of slower flow and are typically smaller in scale than HATs, although some larger models have managed to break into the megawatt range [6].

The blades of both HATs and VATs are known to be susceptible to the fluid-induced instability mechanisms [4, 8]. Specifically, divergence is a static instability which occurs when the deformation-dependent fluid forces overcome structural restoring forces and the effective stiffness of the blade shrinks to zero. Flutter is a dynamic instability that occurs when the natural bending and twisting frequencies of a blade coalesce, resulting in an oscillating response with exponentially increasing amplitude.

VAT blades in particular may be susceptible to three additional types of instabilities. The first is main resonance, which can be excited in VAT blades due to the cyclic nature of fluid loading as the turbine rotates. The second is parametric resonance, which can arise due to the fluid effects

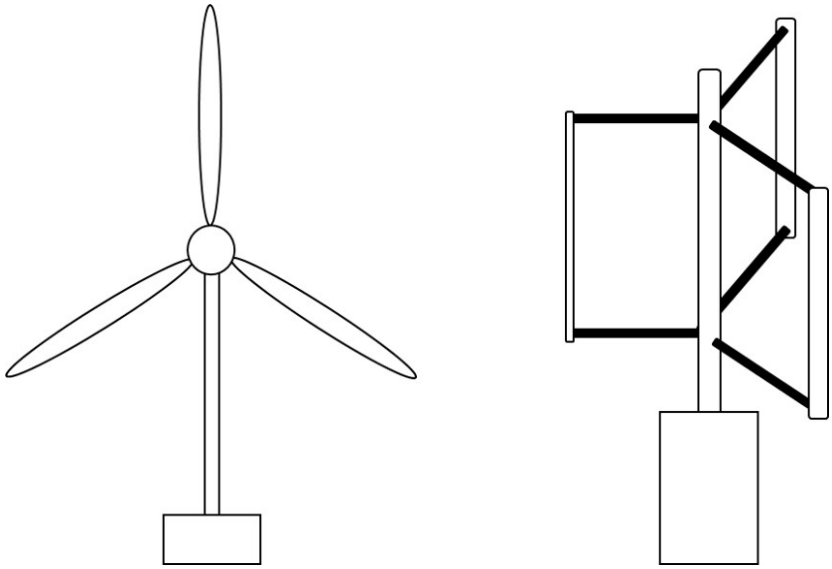

Fig. 1.1. Examples of a horizontal axis turbine (left) and a vertical axis turbine (right)

periodically reducing the effective twisting stiffness of the blade. The third is centrifugal buckling, which occurs when the centrifugal loads on the blade overcome its structural restoring forces. This paper will focus specifically on straight-bladed H-rotor VATs (as shown in Fig. 1.1) due to their simple blade geometry. The medium, wind or water, will not be specified due to the general nature of the model developed later on in this paper, though a range of fluid properties will be explored.

Many modeling techniques exist which are capable of capturing the fluid effects on VAT blades to varying degrees. Among these, Blade Element Momentum Theory, Lifting Line Theory, and Boundary Element Methods are some of the most popular. However, these methods are unsuitable for the present study since they do not typically account for the unsteady effects caused by the oscillations of a flexible blade [12].

Computational Fluid Dynamics (CFD) methods are much more accurate and are generally the most reliable way to capture the nonlinear effects of a real, viscous flow in a finite domain. Various schemes exist for coupling CFD models with structural models to obtain Fluid-Structure Interaction (FSI) simulations. In one study conducted by the International Islamic University in 2018, it was found that simulating a tidal turbine for 0.29 second of operation took 38 processors a minimum of

58.3 hrs, even using the simplest one-way coupling scheme [1]. This indicates that an FSI model would be too computationally expensive for the present study which focuses on qualitative behavior through an investigation of thousands of different conditions.

Unsteady Foil Theories (UFTs) look at the loads generated on a 2D foil in inviscid flow with regular oscillation in both pitching and heaving degrees of freedom (DOFs). These methods offer a compromise between computational efficiency and accuracy, and they have been successfully implemented to model flexible blades in past studies [2, 3, 9].

The approach adopted in this paper is an extension of Theodorsen's UFT into the form of a Finite Element Model (FEM) which includes centrifugal effects [10]. This fluid model was selected for two reasons. First, its relative simplicity allows for the development of an efficient beam-element-style model, essential in the task of exploring a large design space to obtain general insights. Second, this method inherently accounts for some of the dynamic effects of a flexible blade which are key in any analysis of dynamic instabilities.

Theodorsen's model relies on the following assumptions: (a) the flow is inviscid, (b) the vortex shedding frequency is equal to the foil oscillation frequency, (c) the vortices convect downstream parallel to the flow with no dissipation, (d) induced downwash acts at the three-quarter chord point, (e) cavitation/ventilation does not occur [10]. Additionally, since Theodorsen's model is derived for a foil in 2D space, it is necessary to expand the original terms by treating them as distributed loads along the span of the blade. This gives rise to another assumption (f) no induced flow in the spanwise direction. Despite these simplifications, similar approaches utilizing Theodorsen's UFT have been shown to provide good agreement with more exact solutions, even for light foils in relatively dense fluid such as hydrofoils [3].

Recently, Theodorsen's UFT was used in a study of offshore wind turbines [9] where it was also expanded via treatment as distributed loads in the span-wise direction. Natural frequencies, flutter frequencies, and flutter speeds were predicted for three different blade designs: the WindPACT 1.5MW, NREL 5MW, and SNL 100-00. Natural frequencies were compared against six previous studies of the same blades and showed agreement within 6% for five of those studies. Flutter frequencies were compared against five previous studies and showed agreement within 7% for all

five studies. Flutter speeds were also compared against five previous studies and showed agreement within 13% for four of those studies.

1.2 Scope

This paper is organized into six chapters. Chapter 2 is devoted to deriving an FEM model which accounts for structural, fluid, and centrifugal load effects. It starts with an outline of the conventions and assumptions needed to define a 6DOF blade element and then considers each of the three effects (structural, fluid, and centrifugal) in isolation before appending them to the overall model. Chapter 3 discusses the two different solution methods (eigenvalue analysis and time history analysis) used to study the model developed in Chapter 2, as well as the pros and cons of each method. Chapter 4 presents validation studies which are used to assess the accuracy and limitations of the model. In particular, this chapter focuses on assessing how well the model can capture fluid loading effects on the blade by comparing its predictions against experimental measurements of submerged natural frequencies and flutter characteristics. Chapter 5 starts with some simple analytical solutions developed from the model to develop insight. It then considers a single test blade design for which a broad range of operating conditions are tested via both eigenvalue and time history analysis methods. Results are shown in the form of dynamic amplification plots as well as time history and eigenvalue plots for key points of interest. Chapter 6 summarizes the major findings of this paper, reviews potential limitations, and makes suggestions for future study on this topic.

Chapter 2
MODELING

2.1 Overview

This chapter is devoted to developing the model which will be used for the remainder of this paper. First, a 6DOF structural model is developed which accounts for flexure about the blade's weak axis as well as span-wise twisting deformations. Next, the fluid effects will be considered in terms of its static and dynamic components. Finally, centrifugal effects will be appended to the model.

A single governing equation for a 6DOF blade element is presented at the end of this chapter. It should be noted that the computational efficiency benefits gained from the simplicity of this linear formulation are at the cost of excluding nonlinear effects such as wake, span-wise induced flow, and viscosity. This is acceptable since the goal of this paper is a qualitative exploration of the interaction between different instability in VAT blades.

2.2 Conventions and Nomenclature

The model used in this study is in the form of a 6DOF bend-twist-coupled beam element model which accounts for weak-axis flexural as well as span-wise twisting deformations (see Fig. 2.1). Bending deformation, v, is defined positive upwards and twisting deformation, ϕ, is defined positive counter-clockwise (Fig. 2.2). Note that this implies that twisting deformation will have an opposite sense to angle of attack, α, which is traditionally defined positive clockwise for the orientation shown.

All deformations are defined about an assumed elastic axis (E.A.), also sometimes referred to as a center of stiffness. This position is defined such that a transverse load acting through it would cause no twisting on the blade. As shown in Fig. 2.2, the E.A. is located a distance ab behind the

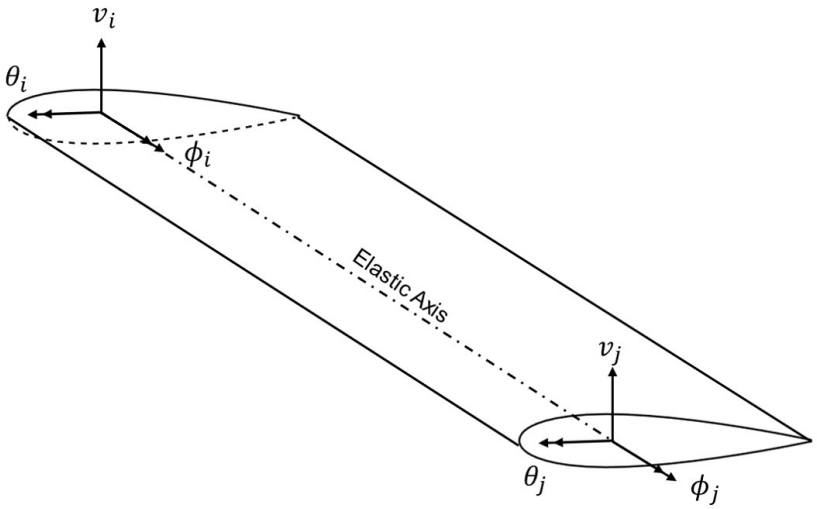

Fig. 2.1. Diagram of a 6DOF beam element

midchord (M.C.) where b is one-half of the chord length, c, and a is a nondimensionalized length scale. The center of gravity (C.G.) is located behind the E.A. a distance of $x_\theta b$. The aerodynamic center (A.C.) is located ahead from the E.A. by a distance of ec. While the use of the two different length scales b and c is somewhat cumbersome, it is necessary in order to align with the conventions established in the current literature.

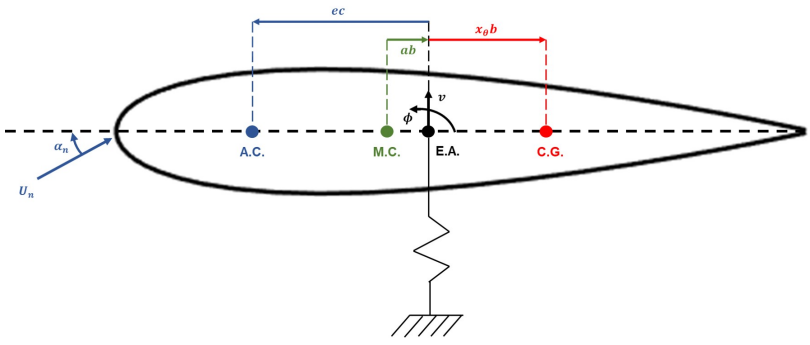

Fig. 2.2. Cross section of the 6DOF beam element defined using terms standard for lifting bodies

Fundamentally, each of the three distances ab, $x_\theta b$, and ec represent lever arms which produce

bend-twist coupling from fluid inertia, structural inertia, and lift forces respectively. By assuming that the A.C. is at its theoretical position of quarter-chord, e can also be defined as $e = 1/4 + a/2$. From this expression it can be observed that there are no possible locations for the E.A. and C.G. which would eliminate all bend-twist coupling in the blade.

2.3 Structural Mechanics

The strong form of the governing equations of motion for weak-axis flexure and twisting are taken as

$$\rho_s A\ddot{v} + EIv'''' = q_{tot}, \tag{2.1}$$

$$\rho_s I_0\ddot{\phi} - GJ\phi'' = t_{tot}, \tag{2.2}$$

where ρ_s is the volumetric density of the blade, A is its cross-sectional area, E is Young's modulus, I is the second moment of area about the weak-axis, I_0 is the polar second moment of area, G is the shear modulus, and J is the torsion constant. Additionally, each dot over a variable represents its partial derivative with respect to time, t, and each apostrophe after a variable represents its partial derivative with respect to span-wise position, x.

Discretization of the governing equations is achieved by applying classical FEM (i.e. obtaining the weak form of Equations (2.1) and (2.2) and the Galerkin assumption to the solution and test functions). Typical flexural and twist shape functions were selected as

$$[N_b]^T = \begin{bmatrix} 1 - 3\left(\frac{x}{L}\right)^2 + 2\left(\frac{x}{L}\right)^3 \\ L\left(\left(\frac{x}{L}\right) - 2\left(\frac{x}{L}\right)^2 + \left(\frac{x}{L}\right)^3\right) \\ 3\left(\frac{x}{L}\right)^2 - 2\left(\frac{x}{L}\right)^3 \\ L\left(\left(\frac{x}{L}\right)^3 - \left(\frac{x}{L}\right)^2\right) \end{bmatrix}, \tag{2.3}$$

$$[N_t]^T = \begin{bmatrix} 1 - \left(\frac{x}{L}\right) \\ \left(\frac{x}{L}\right) \end{bmatrix}, \tag{2.4}$$

where x is spanwise position along the element and L is the length of the element. The deformation of an element can then be expressed as

$$v(x) = [N_b]\{x_b\} \tag{2.5}$$

$$\phi(x) = [N_t]\{x_t\} \tag{2.6}$$

where $\{x_b\}$ is a vector of nodal flexural deformations and $\{x_t\}$ is a vector of nodal twisting deformations. The familiar matrix form of the governing equations was obtained as

$$[M_{bb}]\{\ddot{x}_b\} + [K_{bb}]\{x_b\} = \{P_b\}, \tag{2.7}$$

$$[M_{tt}]\{\ddot{x}_t\} + [K_{tt}]\{x_t\} = \{P_t\}, \tag{2.8}$$

where

$$[M_{bb}] = \int_0^L \rho_s A [N_b]^T [N_b] dx, \tag{2.9}$$

$$[M_{tt}] = \int_0^L \rho_s I_0 [N_t]^T [N_t] dx, \tag{2.10}$$

$$[K_{bb}] = \int_0^L EI [N_b'']^T [N_b''] dx, \tag{2.11}$$

$$[K_{tt}] = \int_0^L GJ [N_t']^T [N_t'] dx, \tag{2.12}$$

$$\{P_b\} = \int_0^L q_{tot} [N_b]^T dx, \tag{2.13}$$

$$\{P_t\} = \int_0^L t_{tot} [N_t]^T dx. \tag{2.14}$$

In order to combine Equations (2.7) and (2.8) into a single governing equation, the inertial coupling between the bending and twisting DOFs caused by the eccentricity between the E.A. and C.G. must be accounted for. Those coupling effects can be separated from q_{tot} and t_{tot} and described by the following equations:

$$q_c = -\ddot{\phi}\rho_s A(x_\theta b), \tag{2.15}$$

$$t_c = -\ddot{v}\rho_s A(x_\theta b), \tag{2.16}$$

where q_c and t_c can be thought of as the external force or torque per unit length required to maintain a pure twisting or pure bending response given a unit acceleration applied at the E.A. They arise when the location at which inertial forces act is artificially shifted from the C.G. to the E.A. in order to align with the element's local coordinate system. Note that these terms go to zero for the special case where the E.A. and C.G. are coincident ($x_\theta = 0$).

Separating q_c and t_c out of the load vectors $\{P_b\}$ and $\{P_t\}$ allows for the following coupled equation of motion

$$\begin{bmatrix} [M_{bb}] & [M_{bt}] \\ [M_{tb}] & [M_{tt}] \end{bmatrix} \begin{Bmatrix} \{\ddot{x}_b\} \\ \{\ddot{x}_t\} \end{Bmatrix} + \begin{bmatrix} [K_{bb}] & [0] \\ [0] & [K_{tt}] \end{bmatrix} \begin{Bmatrix} \{x_b\} \\ \{x_t\} \end{Bmatrix} = \begin{Bmatrix} \{P_{b,fluid}\} \\ \{P_{t,fluid}\} \end{Bmatrix}, \tag{2.17}$$

where the load vectors $\{P_{b,fluid}\}$ and $\{P_{t,fluid}\}$ represent fluid effects and the additional inertial coupling terms can be calculated as

$$[M_{bt}] = \int_0^L \rho_s A(x_\theta b)[N_b]^T[N_t]dx, \tag{2.18}$$

$$[M_{tb}] = \int_0^L \rho_s A(x_\theta b)[N_t]^T[N_b]dx, \tag{2.19}$$

Defining a total structural mass matrix $[M_s]$, total structural stiffness matrix $[K_s]$, and by appending a structural damping matrix $[C_s]$, the final expression representing the structural mechanics of the 6DOF element can be summarized as

$$[M_s]\{\ddot{X}\} + [C_s]\{\dot{X}\} + [K_s]\{X\} = \{P_{fluid}\}, \tag{2.20}$$

where

$$\{X\}^T = \left\{ v_i \ \theta_i \ v_j \ \theta_j \ \phi_i \ \phi_j \right\}. \tag{2.21}$$

2.4 Fluid Mechanics

The fluid loading on the blade is treated as inviscid and decomposed into static and dynamic components:

$$\{P_{fluid}\} = \{P_{static}\} + \{P_{dyn}\}. \tag{2.22}$$

The static component of load is that which arises due to the initial undeformed orientation of the blade with respect to the incoming flow vector. While this is termed static, for VAT blades this term will vary as a function of the blade's position due to the changing angle of attack. Dynamic components of the load are assumed to have a linear dependency on structural deformation $\{X\}$, velocity $\{\dot{X}\}$, or acceleration $\{\ddot{X}\}$ in accordance with Theodorsen's UFT [10].

Static fluid loads on lifting bodies such as blades are typically expressed nondimensionally using terms such as coefficient of lift (C_L) and coefficient of drag (C_D). The redimensionalization of load coefficients requires information about characteristics of the blade, as well as the net angle of attack, α_n, and the net flow speed, U_n. Theoretical values for both of these quantities can be easily calculated according to

$$\alpha_n = -tan^{-1}\left(\frac{sin(\Theta)}{\lambda + cos(\Theta)}\right) + \alpha_p, \tag{2.23}$$

$$U_n = U_\infty \sqrt{\lambda^2 + 2\lambda cos(\Theta) + 1}, \tag{2.24}$$

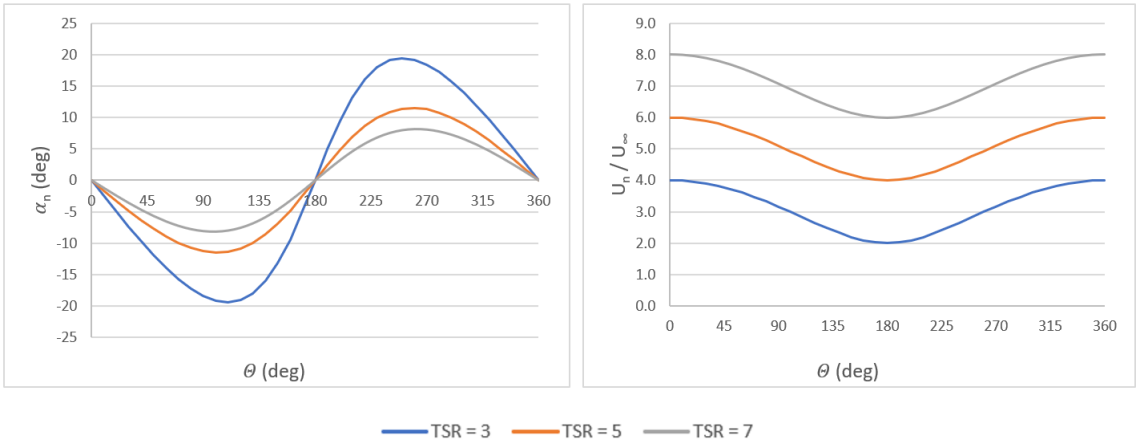

Fig. 2.3. Theoretical values for net angle of attack (left) and net flow speed (right) seen by a VAT blade with $\alpha_p = 0$ over one full rotation at various Tip-Speed-Ratios

where Θ is the azimuthal position of the blade, $\lambda = \frac{\Omega R}{U_\infty}$ is tip-speed-ratio (TSR), Ω is the rotational frequency of the turbine, R is the distance from the blade to the center of rotation, U_∞

is the incoming free-flow speed of the fluid, and α_p is the preset pitch angle measured from the rotational velocity vector, $\overrightarrow{\Omega R}$, to the chordline.

The use of load coefficients is unsuitable for the current study, however, for two main reasons. First, the accuracy of Equations (2.24) and (2.23) is questionable since they neglect important dynamic effects such as the wake of adjacent blades altering the flow field. Second, the high angles of attack seen by VAT blades can lead to dynamic stall which is very difficult to capture in terms of load coefficients.

Thus, a simplified approach is taken whereby the effects of $\{P_{static}\}$ are captured qualitatively. This is done by modeling the weak-axis distributed load, F_{WA}, (which does not identically align with the direction of lift) using a simple sin function

$$F_{WA} = -\left(\frac{1}{2}\rho_f U_{max}^2 c\right)\sin(\Theta), \tag{2.25}$$

where ρ_f is the density of the fluid and U_{max} is the maximum net flow speed seen by the blade. A more detailed comparison between this harmonic approximation and more accurate loading data obtained from 2D CFD analysis is presented in Chapter 4.

With the static component of fluid load now defined as a distributed load, F_{WA}, the static fluid load vector $\{P_{static}\}$ can be obtained as

$$\{P_{static}\} = \begin{Bmatrix} F_{WA}\int_0^L [N_b]^T dx \\ -ecF_{WA}\int_0^L [N_t]^T dx \end{Bmatrix}. \tag{2.26}$$

The dynamic components of fluid loading are modeled after Theodorsen's inviscid formulation for a foil in 2D space [10]

$$\{P_{dyn}^{2D}\} = -[M_f^{2D}]\{\ddot{X}\} - [C_f^{2D}]\{\dot{X}\} - [K_f^{2D}]\{X\}. \tag{2.27}$$

$[M_f^{2D}]$, $[C_f^{2D}]$, and $[K_f^{2D}]$ are Theodorsen's fluid inertial, damping, and stiffness terms. They can be expressed as

$$[M_f^{2D}] = \begin{bmatrix} m_{vv} & m_{v\phi} \\ m_{\phi v} & m_{\phi\phi} \end{bmatrix} = \pi b^2 \rho_f \begin{bmatrix} 1 & -ab \\ -ab & (\frac{1}{8} + a^2)b^2 \end{bmatrix}, \tag{2.28}$$

$$[C_f^{2D}] = \begin{bmatrix} c_{vv} & c_{v\phi} \\ c_{\phi v} & c_{\phi\phi} \end{bmatrix} = 2\pi b\rho_f U_n \begin{bmatrix} C(k) & \frac{b}{2} + b(\frac{1}{2} - a)C(k) \\ -ecC(k) & \frac{b^2}{2}(\frac{1}{2} - a) - ecb(\frac{1}{2} - a)C(k) \end{bmatrix}, \tag{2.29}$$

$$[K_f^{2D}] = \begin{bmatrix} k_{vv} & k_{v\phi} \\ k_{\phi v} & k_{\phi\phi} \end{bmatrix} = 2\pi b\rho_f U_n^2 \begin{bmatrix} 0 & C(k)) \\ 0 & -ecC(k) \end{bmatrix}, \tag{2.30}$$

where $k = \omega_{sys} b/U_n$ is reduced frequency and ω_{sys} is the system oscillation frequency defined by whichever mode has the lowest level of effective damping. The variable $C(k)$ represents Theodorsen's circulation function:

$$C(k) = F(k) + iG(k) = \frac{H_1^2(k)}{H_1^2(k) + iH_0^2(k)}, \tag{2.31}$$

where $H_0^2(k)$ and $H_1^2(k)$ are Hankel functions. It has been shown that $C(k)$ is complex-valued and behaves such that its real part produces a reduction in magnitude and its imaginary part introduces a phase-lag on whatever function it is applied to [9]. This variable will be solved for iteratively via eigenvalue analysis, but only its real part will be considered when performing time history analysis in order to keep deformations real-valued.

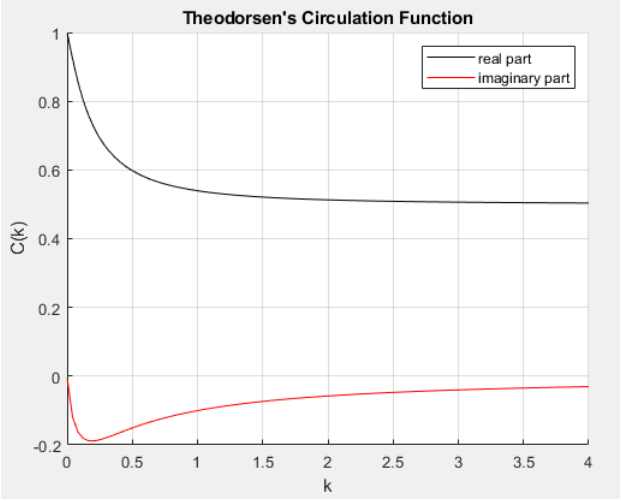

Fig. 2.4. Real and imaginary components of Theodorsen's Function plotted for $0 < k < 4$

In order to implement Theodorsen's 2D UFT within the structural model it is necessary to expand each term into 3D space by treating it as a load per unit span acting on the element. This is convenient for analysis, but notably will ignore finite-span effects such as induced flow in the span-wise direction. Equation (2.32) shows the general framework for expanding each of the above matrices into a suitable form for the 6DOF elements.

$$[A_f] = \begin{bmatrix} a_{vv}\int_0^L [N_b]^T[N_b]dx & a_{v\phi}\int_0^L [N_b]^T[N_t]dx \\ a_{\phi v}\int_0^L [N_t]^T[N_b]dx & a_{\phi\phi}\int_0^L [N_t]^T[N_t]dx \end{bmatrix} \tag{2.32}$$

where L represents the length of the element and a is a placeholder for k, c, or m. This notation is convenient since it is general enough to allow the user to select different shape function for bending or twisting DOFs if desired.

The 6DOF fluid added mass, damping, and stiffness terms ($[M_f]$, $[C_f]$, and $[K_f]$) can be determined using Equation (2.32) in conjunction with the shape functions defined in Equations (2.3) and (2.4). From there, the dynamic component of fluid load can be described as

$$\{P_{dyn}\} = -[M_f]\{\ddot{X}\} - [C_f]\{\dot{X}\} - [K_f]\{X\}. \tag{2.33}$$

Combining Equations (2.20), (2.22) and (2.33) results in a governing equation which accounts for both structural and fluid effects

$$([M_s] + [M_f])\{\ddot{X}\} + ([C_s] + [C_f])\{\dot{X}\} + ([K_s] + [K_f])\{X\} = \{P_{static}\}. \tag{2.34}$$

2.5 Centrifugal Effects

The centrifugal load acting on a unit length of VAT blade as it rotates can be described as

$$F_r = \rho_s A \Omega^2 R_{tot}, \tag{2.35}$$

where R_{tot} is the total distance from center of revolution to the center of mass of the cross-section. Assuming small angles for both preset pitch angle α_p and twisting deformation ϕ, the distance R_{tot} can be split into the following components

$$R_{tot} = R_0 + v + (x_\theta b)\phi, \tag{2.36}$$

where R_0 is the initial undeformed distance between center of revolution and center of mass and the other two terms arise from contributions due to bending and twisting deformation respectively.

Going back to the strong forms of flexure and twisting defined in Equations (2.1) and (2.2) and substituting q_{tot} with F_r and t_{tot} with $(x_\theta b)F_r$ yields

$$\rho_s A\ddot{v} + EIv'''' - \rho_s A\Omega^2 v - \rho_s A\Omega^2(x_\theta b)\phi = \rho_s A\Omega^2 R_0, \tag{2.37}$$

$$\rho_s I_0\ddot{\phi} - GJ\phi'' - \rho_s A\Omega^2(x_\theta b)v - \rho_s A\Omega^2(x_\theta b)^2\phi = \rho_s A\Omega^2(x_\theta b)R_0. \tag{2.38}$$

These expressions demonstrate that centrifugal effects manifest as both an effective stiffness softening as well as an applied steady load. Following the same procedure of descretization used for the structural mechanics of the blade, the bend-twist-coupled centrifugal stiffness matrix $[K_r]$ was obtained as

$$[K_r] = -\Omega^2 \int_0^L \rho_s A \begin{bmatrix} [K^r_{bb}] & [K^r_{bt}] \\ [K^r_{tb}] & [K^r_{tt}] \end{bmatrix}, \tag{2.39}$$

where

$$[K^r_{bb}] = -\Omega^2 \int_0^L \rho_s A [N_b]^T [N_b] dx, \tag{2.40}$$

$$[K^r_{bt}] = -\Omega^2 \int_0^L \rho_s A (x_\theta b) [N_b]^T [N_t] dx, \tag{2.41}$$

$$[K^r_{tb}] = -\Omega^2 \int_0^L \rho_s A (x_\theta b) [N_t]^T [N_b] dx, \tag{2.42}$$

$$[K^r_{tt}] = -\Omega^2 \int_0^L \rho_s A (x_\theta b)^2 [N_t]^T [N_t] dx. \tag{2.43}$$

The steady load vector from centrifugal effects $\{P_r\}$ can be similarly described as

$$\{P_r\} = \Omega^2 \int_0^L \rho_s A R_0 \begin{Bmatrix} [N_b]^T \\ (x_\theta b)[N_t]^T \end{Bmatrix} dx, \tag{2.44}$$

By appending $[K_r]$ and $\{P_r\}$ into Equation (2.34), the final governing equation is obtained which will hereafter be referred to as the "Vertical-Axis Turbine-Blade-Element-Model" (VATBEM)

$$([M_s] + [M_f])\{\ddot{X}\} + ([C_s] + [C_f])\{\dot{X}\} + ([K_s] + [K_f] + [K_r])\{X\} = \{P_{static}\} + \{P_r\}. \tag{2.45}$$

By noting the fact that $[C_f]$, $[K_f]$, and $\{P_f\}$ are all functions of U_n, which is itself a function of time, Equation (2.45) can also be expressed more succinctly as

$$[M]\{\ddot{X}\} + [C(t)]\{\dot{X}\} + [K(t)]\{X\} = \{P(t)\}, \tag{2.46}$$

which emphasizes the fact that the system may be susceptible to both main and parametric resonance.

Chapter 3

SOLUTION METHODS

Two methods are used to study the system defined by Equation (2.46). The first is an eigenvalue analysis which is able to directly predict divergence, flutter, or centrifugal buckling, as well as estimate the the 1st mode bending and twisting frequencies of the system to indirectly predict main and parametric resonance. The second is time history analysis which is used as a more accurate, but also more computationally expensive, method by which main and parametric resonances can be observed directly.

3.1 Eigenvalue Analysis

The following analysis of Equation (2.46) requires two major assumptions. First, that the load vector $\{P(t)\} = \{0\}$ and secondly that all of the system parameters are constant valued and do not vary with time. In this case, time-averaged values for the damping and stiffness matrices are selected ($[C_{avg}]$ and $[K_{avg}]$ respectively).

By following the procedure outlined in [5] the second order differential equation described by Equation (2.46) can be recast into a first order system by first defining the state vector

$$\{Q\} = \begin{Bmatrix} \{X\} \\ \{\dot{X}\} \end{Bmatrix}. \tag{3.1}$$

From there the governing equation can be rewritten as

$$\{\dot{Q}\} = [S]\{Q\}, \tag{3.2}$$

where

$$[S] = \begin{bmatrix} [0] & [I] \\ -[M]^{-1}[K_{avg}] & -[M]^{-1}[C_{avg}] \end{bmatrix}. \tag{3.3}$$

The solution to Equation (3.2) is

$$\{Q(t)\} = [\Phi]e^{[\Lambda](t-t_0)}[\Phi]^{-1}\{Q(t_0)\}, \tag{3.4}$$

where $[\Phi]$ is a matrix containing the right eigenvectors of $[S]$, $[\Lambda]$ is a diagonal matrix containing the eigenvalues of $[S]$, and $t \geq t_0$. Since the solution in Equation (3.4) relies on the assumptions of zero load and constant system properties, it cannot serve as an exact solution to the forced response of the blade. However, it does offer several important insights which make it a useful tool in quickly predicting the stability of the system.

The matrix $[\Lambda]$ contains pairs of eigenvalues λ_i and λ_i^* which are complex-conjugates of each other and describe the displacement and velocity response of a single mode, respectively. The fact that these pairs are complex-conjugates is a general property of the solution method and is necessary to ensure the state-vector $\{Q\}$ remains real-valued.

A system which contains any eigenvalue with a positive real component has negative damping and will be unstable. If that eigenvalue also has a non-zero imaginary component then the instability type is flutter. Otherwise, if the imaginary component is equal to zero then the instability type is either divergence or centrifugal buckling.

Because this method relies on the assumption that $\{P\} = \{0\}$, this method cannot directly capture main resonance. Additionally, because Equation (3.4) assumes that the system damping and stiffness matrices are constant, it is also incapable of directly capturing parametric resonance. It can, however, be used to predict the time-averaged vibrational response of the system by considering the magnitude of the imaginary part of either λ_i or λ_i^* for each mode. Coupled with knowledge about which ratios of response frequency to forcing frequency, ω_0/Ω, are capable of producing main and parametric resonances, this allows us to predict the conditions required for either type of resonance to occur.

Throughout the rest of this paper, eigenvalue analysis is used to determine vibrational response of systems, in iterative calculations of Theodorsen's Function, $C(k)$, and as a computationally cheap method of predicting instabilities.

3.2 Time History Analysis

Newmark's Method is a popular choice for solving the Time History Analysis (THA) of many different kinds of problems in structural engineering. Typically this method is applied to systems where the effective mass, damping, and stiffness are all invariant with respect to time. Therefore, it is prudent to show that this method is still valid for systems with parametric variation such as the one defined in Equation (2.46).

Newmark's Method starts by assuming that the state of a system is known at a given timestep, n. This state is completely described by three vectors, $\{X\}_n$, $\{\dot{X}\}_n$, and $\{\ddot{X}\}_n$. By using the extended mean value theorem, the following equations can be derived to express the velocity and displacement at the next timestep, $n+1$:

$$\{\dot{X}\}_{n+1} = \{\dot{X}\}_n + [(1-\gamma)\Delta t]\{\ddot{X}\}_n + \gamma\Delta t\{\ddot{X}\}_{n+1}, \tag{3.5}$$

$$\{X\}_{n+1} = \{X\}_n + \Delta t\{\dot{X}\}_n + \left[\left(\frac{1}{2}-\beta\right)\Delta t^2\right]\{\ddot{X}\}_n + \beta\Delta t^2\{\ddot{X}\}_{n+1}, \tag{3.6}$$

where γ and β are quadrature parameters bounded by $0 \leq \gamma \leq 1$ and $0 \leq 2\beta \leq 1$. It has been shown that $\gamma = 1/2$ is the only value which does not induce artificial damping into the predicted response of the system. Defining $\beta = 1/4$ is often referred to as the average constant acceleration scheme and is a popular choice because it can guarantee unconditional stability. However, for this work $\beta = 1/12$ is selected because it has been shown to minimize error in the frequency response of the system [7].

Equations (3.5) and (3.6) are based purely on kinematic relationships and are not affected by the nature of system mass, damping, or stiffness. The third equation needed to derive Newmark's Method is simply the governing equation itself evaluated at $n+1$

$$[M]_{n+1}\{\ddot{X}\}_{n+1} + [C]_{n+1}\{\dot{X}\}_{n+1} + [K]_{n+1}\{X\}_{n+1} = \{P\}_{n+1}. \tag{3.7}$$

Combining Equations (3.5)-(3.7) yields

$$\{X\}_{n+1} = [\tilde{K}]^{-1}\{\tilde{P}\}, \tag{3.8}$$

where

$$[\tilde{K}] = [K]_{n+1} + \frac{\gamma}{\beta\Delta t}[C]_{n+1} + \frac{1}{\beta\Delta t^2}[M]_{n+1}, \tag{3.9}$$

$$\{\tilde{P}\} = \{P\}_{n+1} + [a_1]\{X\}_n + [a_2]\{\dot{X}\}_n + [a_3]\{\ddot{X}\}_n, \tag{3.10}$$

$$[a_1] = \frac{1}{\beta\Delta t^2}[M]_{n+1} + \frac{\gamma}{\beta\Delta t}[C]_{n+1}, \tag{3.11}$$

$$[a_2] = \frac{1}{\beta\Delta t}[M]_{n+1} + \left(\frac{\gamma}{\beta} - 1\right)[C]_{n+1}, \tag{3.12}$$

$$[a_3] = \left(\frac{1}{2\beta} - 1\right)[M]_{n+1} + \Delta t\left(\frac{\gamma}{2\beta} - 1\right)[C]_{n+1}. \tag{3.13}$$

The result is convenient but slightly counter-intuitive, showing that the displacement at $n+1$ can be determined without relying on any information about the system properties at n.

A single DOF system capable of experiencing parametric resonance can be defined as follows

$$\ddot{x} + 2\xi\omega_0\dot{x} + \omega_0^2\left[1 + \delta cos(\Omega t)\right]x = 0, \tag{3.14}$$

where ω_0 is the average free response frequency of the system, δ is a nondimensional term which controls the amplitude of parametric variation, Ω is the frequency of parametric variation, and ξ is the critical damping factor of the system.

The system described by Equation (3.14) will be used as an example in order to (a) ensure that the Newmark Method can capture the phenomenon of parametric resonance and (b) determine the maximum allowable value the timestep interval, Δt, can take relative to the natural period of the system, T.

Based on the results of a convergence study shown in Fig 3.1, it has been determined that Newmark's Method is capable of accurately capturing parametric resonance and that 100 or more timesteps per period are required to reach sufficient convergence. (Note that for multiple degree-of-freedom systems, the largest timestep will be a function of the shortest period of the system [7]). This is well-above both the theoretical convergence and stability requirements for $\beta = 1/12$ defined by Equations (3.15) and (3.16) and derived in [7].

$$\frac{T}{\Delta t} \geq 2\pi\sqrt{\beta} \approx 1.8, \tag{3.15}$$

$$\frac{T}{\Delta t} \geq \pi\sqrt{1-4\beta} \approx 2.6, \tag{3.16}$$

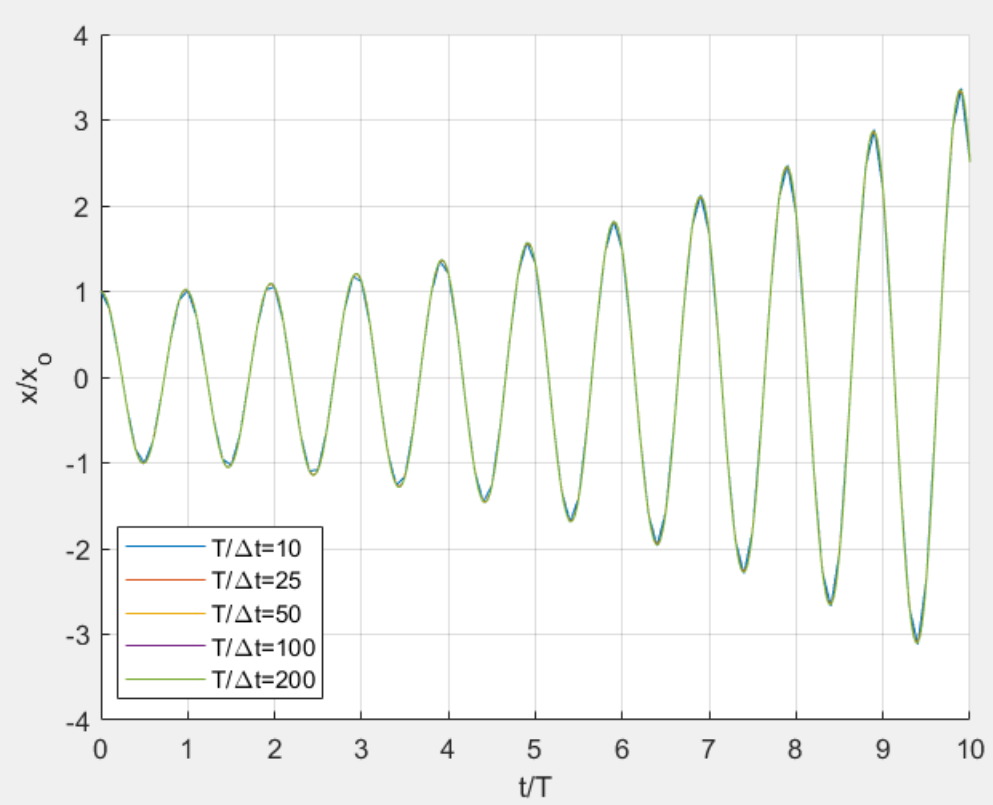

Fig. 3.1. Convergence study preformed on the system described by Equation (3.14) using $\omega_0 = 0.5$, $\Omega = 1$, and $\delta = 0.1$

Additionally, a Strutt Diagram has been constructed (Fig 3.2) to show the ability of Newmark's Method to capture higher modes of parametric resonance as well as highlight the effect of damping. This was done by taking one million THAs over a domain of 1000 ω_0/Ω ratios by 1000 values of δ. Each THA was run for 100 cycles with 100 timesteps per cycle. The ratio of the max displacement, x_{max}, over an initial perturbation, x_0, was then taken from each THA. Fig 3.2 shows the results as a series of overlayed contour maps where enclosed areas are regions of instability defined by $x_{max}/x_0 \geq 100$. Note that all three of the resonance bands for $\xi = 0$ should theoretically touch the x-axis at integer values of $2\omega_0/\Omega$. The fact that they do not comes from the limitations due to the

coarseness of the 1000x1000 search space and the length of each THA.

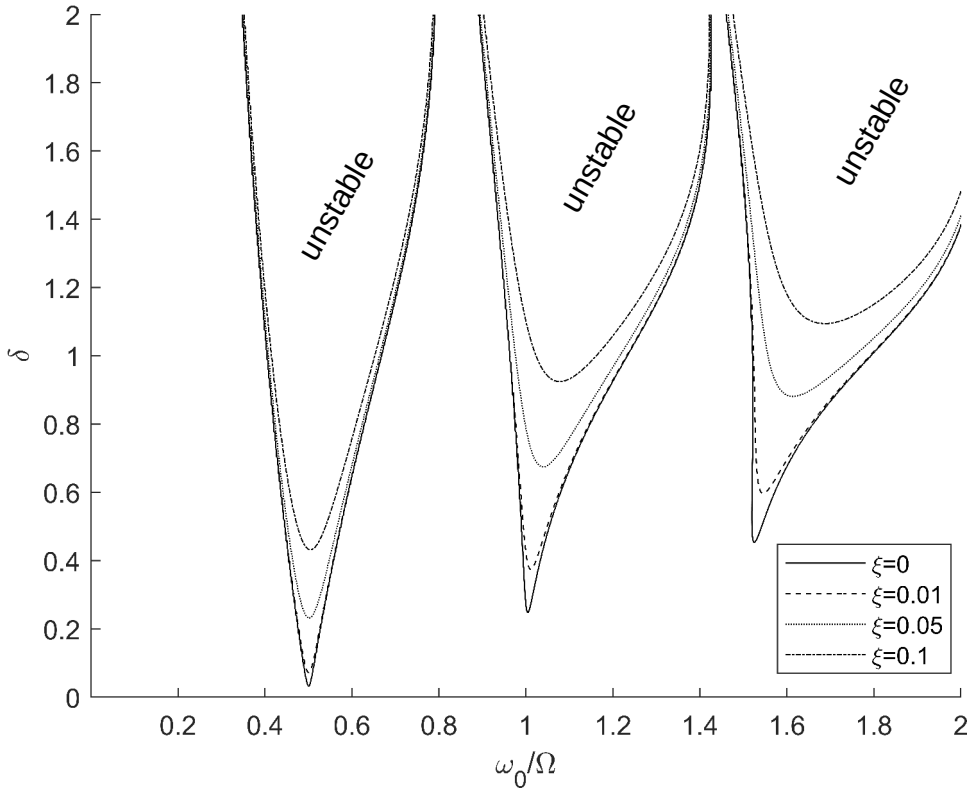

Fig. 3.2. A Strutt Diagram constructed using Newmark-Beta time-integration.

It is interesting to note that a horizontal line at $\delta = 1$ would represent the boundary where systems above that line experience negative stiffness for a portion of each parametric cycle. Contrary to what intuition might predict, the Strutt Diagram shows that it is possible to have systems above this line remain stable globally despite experiencing instantaneous loss of stiffness.

Chapter 4
VALIDATION

At this point it is useful to look at each component of the model individually. The VATBEM model described by Equation (2.45) consists of seven matrices and two load vectors. To the extent possible, each term is validated in isolation against results available in the literature. Note that each of the several blade designs and test conditions discussed in this chapter are considered for validation only and will not be carried forward into Chapter 5.

4.1 Fluid Added-Mass

By looking at the components of each fluid matrix, it can be seen that the fluid added-mass matrix, $[M_f]$, is the only term which is independent of flow speed. Therefore, its accuracy can be confirmed by looking at how the model predicts free-vibration of a beam submerged in still fluid.

The authors of [2] collected experimental data on a flexible cantilevered foil to validate their viscous loose hybrid coupled model. Measurements were made of the 1st, 2nd, and 3rd modal frequencies of a cantilevered NACA0015 POM hydrofoil in-air and in-still-water using impulse excitations and an electrodynamic shaker. The reported properties of the hydrofoil are shown in Table 4.1.

Four additional properties were required to validate the VATBEM model presented in this paper. The cross-sectional area ($10.2cm^2$) and polar moment of inertia ($58.6cm^4$) of the NACA0015 foil were calculated in MATLAB using an application of the Divergence Theorem. The weak-axis second moment of inertia ($1.54cm^4$) and torsion constant ($6.96cm^4$) were determined by minimizing the error with respect to experimental frequencies reported for in-air measurements. The remaining errors of the calibrated model were -5% for 1st mode (bending), 0% for 2nd mode (twisting), and +5% for 3rd mode (bending).

Table 4.1. Properties of the flexible hydrofoil used in Chae et al. (2016)

Property	Variable	Value
Foil Type	-	NACA0015
Chord	c	0.1m
Span	L	0.191m
Material Density	ρ_s	$1420 kg/m^3$
Young's Modulus	E	2.9 GPa
Poisson's Ratio	ν	0.35
Structural Damping Ratio (1st mode tending)	ξ_v	2%
Structural Damping Ratio (1st mode twisting)	ξ_ϕ	2%
Nondimensional Distance from M.C. to E.A.	a	-0.28
Nondimensional Distance from E.A. to A.C.	e	0.11
Nondimensional Distance from E.A. to C.G.	x_θ	0

These parameters (calibrated to match in-air measurements) were then fed into the VATBEM model and used to predict the vibrational response of the flexible hydrofoil in-still-water. The results listed in Table 4.2 show that the model can accurately capture the effects of fluid-added-mass for the first bending and twisting mode of the blade, but that accuracy may fall off quickly at higher modes where effects like shear deformation, ventilation, and span-wise induced flow may become more relevant.

Table 4.2. Eigenvalue analysis predictions for frequencies of a flexible hydrofoil in-still-water

Mode	Measured Frequency (Hz)	Predicted Frequency (Hz)	Percent Error
1 (Bending)	34	33	3%
2 (Twisting)	184	182	1%
3 (Bending)	292	221	24%

4.2 Fluid added-damping and added-stiffness

The accuracy of the fluid-added stiffness and damping matrices $[K_f]$ and $[C_f]$ is verified by comparing the model's predictions against experimental measurements of flutter speed and frequency obtained in [11] where nine flexible, cantilevered blade design were tested over a range of fluid densities to determine the influence of an added mass ratio $\left(\sqrt{\mu_b} = \sqrt{\rho_s A/\pi\rho_f b^2}\right)$ on the speed at which flutter occurs. Three blade designs were selected for use in this validation study. The model IDs of these designs are 17-32-4, 27-38-4, and 27-31-4 where the first and second numbers indicates the approximate location of the E.A. and C.G. respectively, and the last number represents the ratio of wing span to chord length. The chord length of all models was 0.3m, the foil shape was NACA 16-010, and all blades were constructed with balsa wood and a single stiffening spar used to alter the location of the E.A.

All additional properties needed for validation were obtained from measured values listed in Table 1 of [11]. A comparison between the flutter speeds and frequencies measured in [11] and those predicted using eigenvalue analysis of the VATBEM model is shown for all three blades in Fig. 4.1. A discrepancy can be observed for all three blades where the eigenvalue analysis starts to overpredict the flutter speed and eventually fails to detect flutter at all for $\sqrt{\mu_b} < 2$. This discrepancy is known to be characteristic of linear models such as VATBEM. A more detailed discussion can be found in [3] which attributes dynamic instability for $\sqrt{\mu_b} < 2$ to an entirely different mechanism dubbed 'dynamic divergence' which can only be captured through nonlinear analysis.

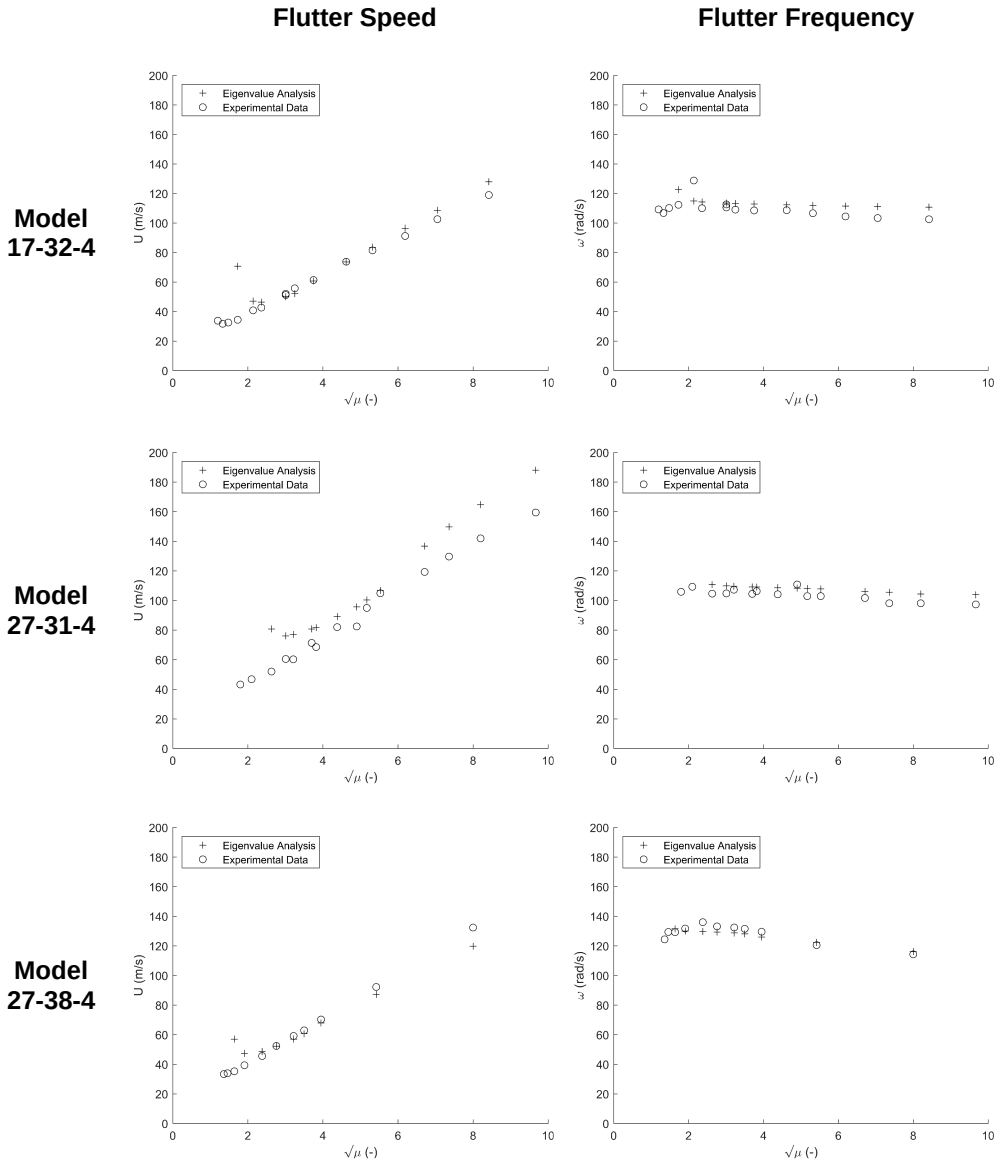

Fig. 4.1. Flutter speed and frequency predictions made using eigenvalue analysis validated against experimental results.

4.3 Static Fluid Load

The the static component of fluid load $\{P_{static}\}$ described by Equations (2.25) and (2.26) is compared against a single set of data obtained by the University of Wisconsin-Madison, Department of Engineering Physics which performed 2D CFD analysis to obtain the pressure field on a foil as it rotates around a central shaft. Two blades were simulated with 180 degree separation from one another, the foil shape is NACA0018 with a preset pitch angle of 6 degrees and a Reynolds of 45,000 in order to model marine flow conditions. Additionally, the 2D CFD analysis assumes a chord-to-radius ratio of 0.47 and a TSR of 1.9. The results of this modelling effort were post-processed to obtain an effective load per unit span acting on the weak axis of the blade. Phase-averaged results are shown in Fig. 4.2 along with a comparison against the assumed F_{WA}.

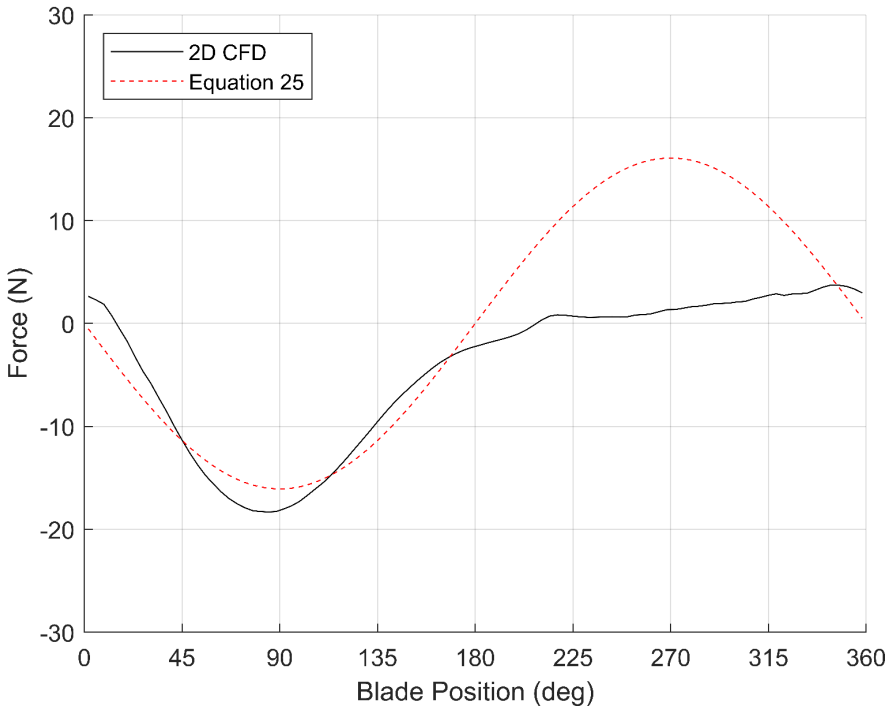

Fig. 4.2. Comparison of the assumed force acting on the weak axis of the blade against 2D CFD

The true behavior of static fluid loads on a blade of a 2-bladed VAT at low Reynolds Numbers

and low TSR is quite different from a simple sin wave. Nonlinear effects can be seen to greatly impact these loads for the down-washed region of $180^o \leq \Theta \leq 360^o$. The exact nature of these effects will vary strongly with parameters such as preset pitch angle, Reynolds Number, TSR, chord-to-radius ratio, and the number of blades. It is beyond the scope of this paper to attempt to account for all of these effects.

It should be noted that the only instability which will be affected by this assumption is main resonance since the rest occur due to effects captured in the net mass, damping, and stiffness matrices. Additionally, the assumed shape of $\{P_{static}\}$ over a cycle will not effect the presence or absence of a main resonance response so long as the true nature of $\{P_{static}\}$ is still periodic.

Chapter 5

RESULTS

Prior to exploring the numerical results obtained from the VATBEM model, it is useful to look at closed-form solutions which can be obtained for the two static instabilities: divergence and centrifugal buckling. A 2-element model is employed with full fixity at both ends. This system will have 9 DOFs (v_1,θ_1,ϕ_1,v_2,θ_2,ϕ_2,v_3,θ_3,and ϕ_3) but only two of them will be free to displace (v_2 and ϕ_2). θ_2 represents the span-wise slope at midspan and is zero by argument of symmetry. For numerical studies, θ_2 was free to displace and higher-element models were also explored.

5.1 Divergence of a Stationary Blade

The conditions necessary for divergence of a stationary blade are easily obtained from the 2-element model by setting $\Omega = 0$ and solving $det([K_{2x2}]) = 0$. Doing this, the following expression is obtained

$$U_d = C_\phi \sqrt{\frac{GJ}{\pi \rho_f e c^2 L^2}} \tag{5.1}$$

where U_d is the divergence flow speed and C_ϕ is a numerical constant determined by boundary conditions. In this case, $C_\phi = \sqrt{12}$, however in Appendix A it is shown that $C_\phi = \pi$ for the exact solution of a blade with both ends fully-fixed. Equation (5.1) matches the form we should expect given similar equations such as those derived in [3]. Note that the term $C(k)$ does not appear in Equation (5.1) since $C(k) = 1$ for the static limit.

5.2 Centrifugal Buckling in a Vacuum

Centrifugal Buckling is another method by which the effective stiffness of the system may go to zero. An assumption is made that the E.A. and C.G. are coincident to help simplify the solution

(i.e. $x_\theta = 0$). The rotational speed required to reach centrifugal buckling in a vacuum, Ω_c, can then be determined by setting $\rho_f = 0$ and again solving $det([K_{2x2}]) = 0$

$$\Omega_c = C_v \sqrt{\frac{EI}{\rho_s A L^4}} \tag{5.2}$$

where Ω_c is the rotational speed required to excite centrifugal buckling and C_v is another numerical constant determined by boundary conditions and shape functions. In this case $C_v \approx 22.7$ for the 2-element model. The strong-form solution is shown to be $C_v \approx 22.2$ in Appendix B.

5.3 Nondimensionalization

The solutions presented in Equations 5.1 and 5.2 offer a natural scheme for normalization whereby nondimensional flow-speed and turbine speed can be represented as

$$U^* = U \sqrt{\frac{\pi \rho_f e c^2 L^2}{GJ}}, \tag{5.3}$$

$$\Omega^* = \Omega \sqrt{\frac{\rho_s A L^4}{EI}}. \tag{5.4}$$

Together, these two terms are used to completely describe the operating state of the VAT blade being modeled. It should be noted that U^* represents a normalization of the free flow speed of the fluid as opposed to the net flow speed on the blade.

5.4 Numerical Solutions

A numerical study was conducted on a 2-element fix-fix blade over a domain of $0 \leq \Omega^* \leq 25$ and $0 \leq U^* \leq 4$ in order to study its stability over the entire range of statically stable operating conditions. The properties listed in Table 5.1 were chosen to represent typical values for a solid NACA0018 blade made with standard uni-directional carbon fiber. The torsion constant of the blade was reduced from an initial value of $J = 1.01x10^{-4}m^4$ in order to ensure that twisting resonance bands would be contained within the statically stable region.

Table 5.1. Numerical study parameters

Property	Variable	Value
Turbine Radius	R	$1.35m$
Blade Length	L	$2.42m$
Chord Length	c	$0.64m$
Area	A	$5.04x10^{-2}m^2$
Polar Second Moment of Area	I_0	$1.10x10^{-3}m^4$
Weak-Axis Second Moment of Area	I	$3.81x10^{-5}m^4$
Torsion Constant	J	$2.52x10^{-6}m^4$
Blade Density	ρ_s	$1600kg/m^3$
Fluid Density	ρ_f	$1kg/m^3$
Young's Modulus	E	$135GPa$
Poisson's Ratio	ν	0.30
Structural Damping Ratio (1st-mode bending)	ξ_v	5%
Structural Damping Ratio (1st-mode twisting)	ξ_ϕ	5%
Nondimensional Distance from M.C. to E.A.	a	-0.30
Nondimensional Distance from E.A. to A.C.	e	0.10
Nondimensional Distance from E.A. to C.G.	x_θ	0

Eigenvalue analysis was performed in order to predict divergence, flutter, and centrifugal buckling boundaries along with contour lines showing where resonance bands should be expected to occur. A suite of THAs was then performed over thousands of discrete combinations of Ω^* and U^* in order to capture dynamic amplification effects over the entire domain of operating conditions.

Two different dynamic amplification factors were obtained from each individual THA. The dynamic bending amplification factor, DAF_v, and dynamic twisting amplification factor, DAF_ϕ, were both calculated as follows

$$DAF_v = v_{max}/v_{static} \tag{5.5}$$

$$DAF_\phi = \phi_{max}/\phi_{static} \tag{5.6}$$

where v_{max} and ϕ_{max} are the maximum bending and twisting displacements predicted over the course of the THA and v_{static} and ϕ_{static} were solved according to

$$\begin{Bmatrix} v_{static} \\ \phi_{static} \end{Bmatrix} = [K_{max}]^{-1}\{P_{max}\} \tag{5.7}$$

where $[K_{max}]$ contains the maximum values of stiffness components and $\{P_{max}\}$ contains the maximum values of load on the blade. This definition was adopted out of necessity due to the fact that the average effective stiffness of the system was less than or equal to zero for many of the operating conditions sampled.

The results of both the eigenvalue analysis and the suite of THAs are presented in Fig. 5.1. It should be noted that despite the normalization of flow speed against ρ_f, e, c, L, G, and J, and turbine speed against ρ_s, A, L, E, and I, variations in any single parameter can drastically alter the shape of the stability landscape shown in Fig. 5.1. This arises due to nonlinear combinations of those parameters in the fully-coupled model.

The closed-form solution obtained for the limit of centrifugal buckling of a VAT blade in a vacuum matches closely with that for a VAT blade under operating conditions in both eigenvalue and time history analyses. Divergence was predicted to occur at a specific value of net flow speed. The eigenvalue analysis shows the divergence boundary as a function of both U^* and Ω^* since both are needed to determine the net flow speed on the blade. The eigenvalue analysis also predicted that

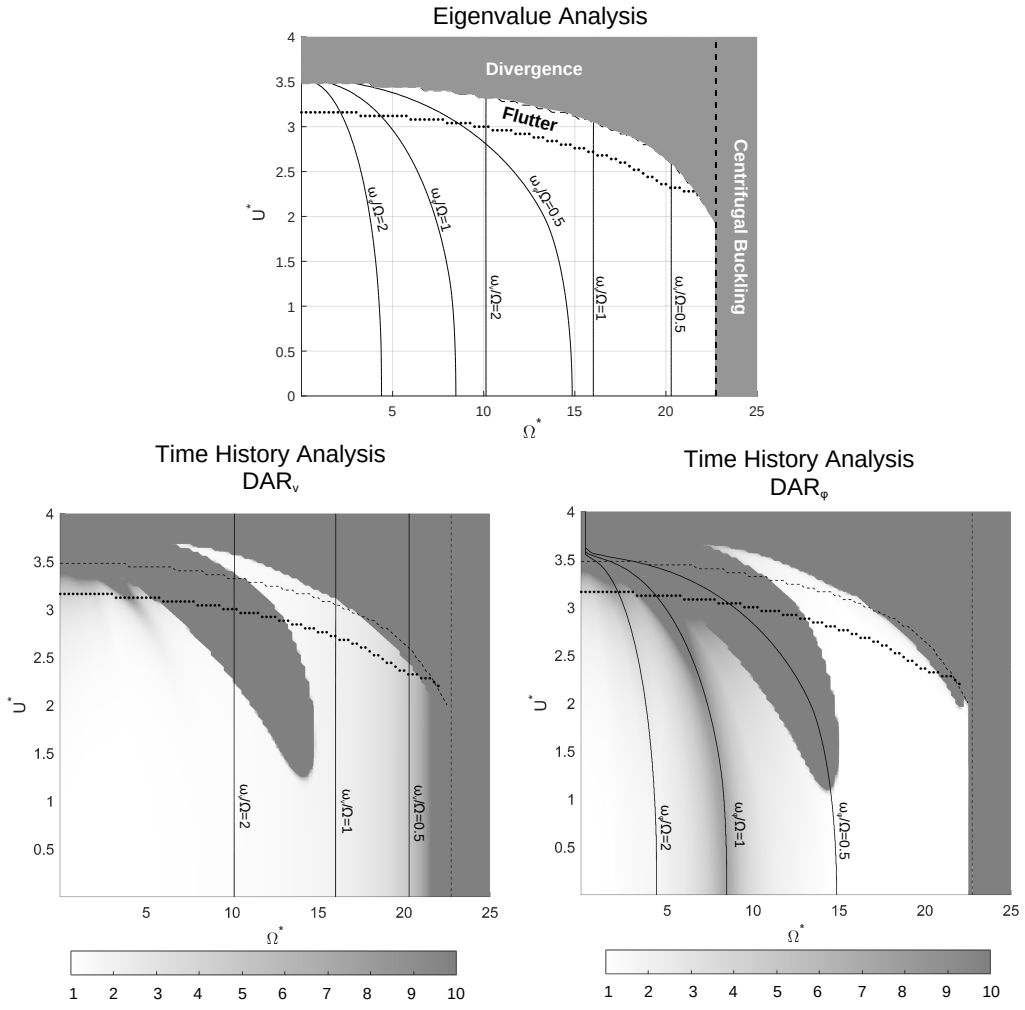

Fig. 5.1. Top: Eigenvalue Analysis results. Bottom Left: THA results showing the DAR_v and 3 possible bending resonance lines. Bottom Right: THA results showing the DAR_ϕ and 3 possible twisting resonance lines

flutter would occur slightly before divergence for most values of Ω^*. A discrepancy can be observed between the boundaries predicted via eigenvalue analysis and the stability boundary shown from THA. Further analysis of the results revealed that the THA was not capturing flutter occurring anywhere within the domain of $0 \leq \Omega^* \leq 25$ and $0 \leq U^* \leq 4$. This is likely due to the omission of the imaginary component of $C(k)$ when performing the time integration.

However, even given this limitation, it is still surprising that the system would remain stable past the divergence boundary. Fig. 5.2 shows a portion of the THA results as well as an eigenvalue plot produced in order to better understand what is going on at key points of Fig. 5.1. The conditions $\Omega^* = 9.5, U^* = 3.5$ produce an eigenvalue plot which confirms the that system experiences negative damping for the majority of each load cycle, while the THA results show a globally stable response. Further investigation is required to better understand the cause of this unexpected "parametric stabilization" in predominately statically unstable conditions.

Main resonance is clearly observed with respect to the twisting frequency of the blade along the contour line $\omega_\phi/\Omega = 1$. Surprisingly, main resonance is not observed anywhere in Fig. 5.1 with respect to the bending frequency of the blade. This result is unexpected since the load vector $\{P_{fluid}\}$ applies sinusoidal forcing to both twisting and bending DOFs in the blade. Further investigation reveals that main bending resonance does not appear in Fig. 5.1 because the bending response of the system is dominated by the steady loads captured in $\{P_{rot}\}$. It is found that main bending resonance does amplify the deformation caused by $\{P_{static}\}$, however this term accounts for less than 1% of the total deformation in areas where main bending resonance would occur which is why the net DAR_v does not exceed a value of 1.05.

Both twisting and bending dynamic amplification factors point to a strong 1st-mode twisting parametric resonance response occurring around the $\omega_\phi/\Omega = 0.5$ contour line. Additionally, faint twisting resonance bands can be observed in both DAF_v and DAF_ϕ for higher modes of twisting parametric resonance. These are fainter due to the increasing influence of damping at higher modes. No parametric resonances are observed with respect to the bending frequency of the blade, regardless of which DAF is considered. This result is unsurprising considering that the bending frequency of the system does not vary parametrically with time.

Centrifugal Buckling
$\Omega^* = 23$
$U^* = 0$

Main Resonance
$\Omega^* = 8.0$
$U^* = 1.4$

Parametric Resonance
$\Omega^* = 13$
$U^* = 2.1$

Divergence
$\Omega^* = 19$
$U^* = 2.8$

Parametric Stabilization
$\Omega^* = 9.5$
$U^* = 3.5$

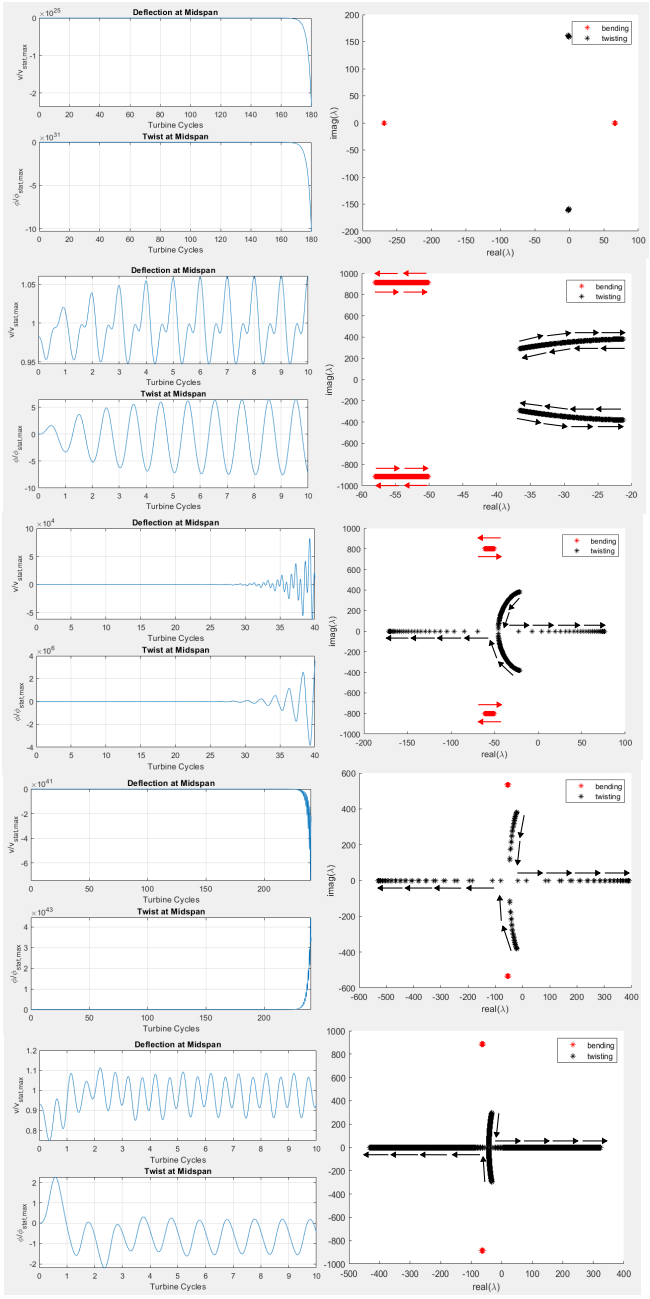

Fig. 5.2. Time history results and eigenvalue plots for points of interest

Chapter 6

CONCLUSION

This paper uses finite element methods in conjunction with Theodorson's Unsteady Flow Theory to predict the behavior of five different types of instability in vertical axis turbine blades. The validity of the FEM model was tested against various sources in the literature where it was found to preform well at predicting the 1st mode bending and twisting frequencies of a submerged blade. Additionally, comparisons were made against experiments preformed in [11] showing that the model was capable of accurately predicting the flutter response of a blade for $\sqrt{\mu_b} > 2$.

Two parameters were used to quantify the operating state of the VAT: nondimensional flow speed, U^*, and nondimensional turbine speed, Ω^*. Centrifugal buckling was found to occur at a single value of Ω^* regardless of the flow speed. Main and parametric resonances were predicted via eigenvalue analysis and confirmed using time history analysis. Strong parametric resonance and main resonance responses were observed with respect to twisting, while neither type of resonance was observed with respect to bending. Predictions made for divergence and flutter via eigenvalue analysis were shown to differ substantially from the time history analysis. For flutter, this discrepancy is due to the limited applicability of Theodorsen's function within the time-domain. For divergence, this difference appears to be caused by an unexpected region of "parametric stabilization".

It should be noted that the omission of nonlinear terms from the fluid model may have a significant effect on all of the instabilities studied within this paper, especially for conditions of low TSR where the small angle assumption breaks down. Future work is required to determine the sensitivity of main resonance bands with respect to the shape of the function used to model the static component of fluid load. Additionally, inclusion of nonlinear terms in the dynamic component of fluid load may significantly impact the presence of twisting parametric resonance, the absence of

bending parametric resonance, and the boundaries for divergence and flutter. Therefore, the results obtained in this paper should be considered primarily as qualitative findings with the goal to provide insight and guide future studies.

BIBLIOGRAPHY

[1] Mujahid Badshah, Saeed Badshah, and Kushsairy Kadir. Fluid structure interaction modelling of tidal turbine performance and structural loads in a velocity shear environment. *Energies*, 11(7), 2018.

[2] Eun Jung Chae, Deniz Tolga Akcabay, Alexandra Lelong, Jacques Andre Astolfi, and Yin Lu Young. Numerical and experimental investigation of natural flow-induced vibrations of flexible hydrofoils. *Physics of Fluids*, 28(7):075102, 2016.

[3] Eun Jung Chae, Deniz Tolga Akcabay, and Yin Lu Young. Dynamic response and stability of a flapping foil in a dense and viscous fluid. *Physics of Fluids*, 25, 10 2013.

[4] Khazar Hayat, Alvaro Gorostidi Martinez de Lecea, Carlos Donazar Moriones, and Sung Kyu Ha. Flutter performance of bend–twist coupled large-scale wind turbine blades. *Journal of Sound and Vibration*, 370:149–162, 2016.

[5] Christopher Hoen and Vetco Aibel As. An engineering interpretation of the complex eigensolution of linear dynamic systems. In *23rd Conference and Exposition on Structural Dynamics 2005*, Orlando, Florida, USA, 2005. Society for Experimental Mechanics.

[6] Erik Möllerström, Paul Gipe, Jos Beurskens, and Fredric Ottermo. A historical review of vertical axis wind turbines rated 100 kw and above. *Renewable and Sustainable Energy Reviews*, 105:1–13, 2019.

[7] Nathan M Newmark. A method of computation for structural dynamics. *Journal of the engineering mechanics division*, 85(3):67–94, 1959.

[8] David Popelka. Aeroelastic stability analysis of a darrieus wind turbine. Report SAND82-0672, Sandia National Laboratories, Albuquerque, NM, 1982.

[9] Pariya Pourazarm. *Theoretical Modeling, Experimental Observation, and Reliability Analysis of Flow-induced Oscillations in Offshore Wind Turbine Blades*. PhD thesis, University of Massachusetts Amherst, Amherst, MA, 2016.

[10] Theodore Theodorsen. General theory of aerodynamic instability and the mechanism of flutter. Report No. 496, NASA, Washington, D.C. 20546, 6 1935.

[11] Donalds Woolston, George, and E Castile. Some effects of variations in several parameters including fluid density on the flutter speed of light uniform cantilever wings. Technical Note 2558, Langley Aeronautical Laboratory, Langley Field, VA, 1951.

[12] Yin Lu Young, Michael R. Motley, Ramona Barber, Eun Jung Chae, and Nitin Garg. Adaptive composite marine propulsors and turbines: Progress and challenges. *Applied Mechanics Reviews*, 68, 11 2016.

Appendix A

STRONG-FORM SOLUTION FOR DIVERGENCE OF A STATIONARY BLADE

Starting from the strong form of the equation of motion for twisting and considering static lift forces yields

$$\rho_s I_0 \ddot{\phi} - GJ\phi'' = -\frac{1}{2} ec^2 \rho_f U^2 C_L, \tag{A.1}$$

where $C_L = 2\pi\alpha_n$ is the theoretical coefficient of lift for small angles of attack. The net angle of attack, α_n, can be defined as a function of twist deformation, ϕ, such that

$$\alpha_n = \alpha_0 - \phi \tag{A.2}$$

where α_0 is the initial angle of attack on the undeformed blade. Substituting this definition into Equation (A.1) and considering the static limit where $\ddot{\phi} = 0$ yields

$$GJ\phi'' + \beta\phi = \beta\alpha_0, \tag{A.3}$$

where $\beta = \pi ec^2 \rho_f U^2$. The homogeneous part of Equation (A.3) can be solved explicitly using the following boundary conditions

$$\text{Case 1:} \quad \phi(0) = \phi_i \quad \phi(L) = 0$$

$$\text{Case 2:} \quad \phi(0) = 0 \quad \phi(L) = \phi_j$$

to obtain the following custom shape functions for the twisting DOFs of the blade element

$$N_1(x) = csc\left(\sqrt{\frac{\beta L^2}{GJ}}\right) sin\left(\left(1 - \frac{x}{L}\right)\sqrt{\frac{\beta L^2}{GJ}}\right) \tag{A.4}$$

$$N_2(x) = csc\left(\sqrt{\frac{\beta L^2}{GJ}}\right) sin\left(\left(\frac{x}{L}\right)\sqrt{\frac{\beta L^2}{GJ}}\right). \tag{A.5}$$

The derivatives of these shape functions can then be integrated to obtain a custom twisting stiffness matrix defined as

$$[K_{custom}] = \frac{\sqrt{\beta GJ}}{sin\left(\sqrt{\frac{\beta L^2}{GJ}}\right)}\begin{bmatrix} cos\left(\sqrt{\frac{\beta L^2}{GJ}}\right) & -1 \\ -1 & cos\left(\sqrt{\frac{\beta L^2}{GJ}}\right) \end{bmatrix}. \tag{A.6}$$

Note that even though $[K_{custom}]$ is symmetric, it does not satisfy nodal equilibrium via the columns summing to zero as they would in an ordinary structural system. This is because the solution is describing a non-conservative system where external loads are being treated as internal due to the fluid load's dependence on structural deformation. Additionally, taking the limit of Equation (A.6) as $\beta \rightarrow 0$ is physically equivalent to considering a flow of zero density and yields the traditional twisting stiffness matrix.

The static instability of divergence can now be obtained for a fully-fixed blade by using $[K_{custom}]$ to set up a 2-element model. Because $[K_{custom}]$ is derived from the exact solutions for the shape functions of this system, the results of this 2-element model represent the exact solution.

Setting up the 2-element model and eliminating fixed DOFs yields the following 1x1 stiffness matrix

$$[K_{ff}] = 2\sqrt{\beta GJ}\, cot\left(\sqrt{\frac{\beta L^2}{4GJ}}\right) \tag{A.7}$$

Evaluating the limit of Equation (A.7) as $\beta \rightarrow 0$ yields $4GJ/L$ and is therefore not a condition of instability. The static instability of divergence is only obtained if the following condition is met

$$\sqrt{\frac{\beta L^2}{4GJ}} = \left(n - \frac{1}{2}\right)\pi \qquad\qquad n = 1, 2, 3.... \tag{A.8}$$

By taking $n = 1$ and substituting back in the definition for β, Equation (A.8) can be rearranged to show that the flow speed required to elicit divergence in a fully-fixed blade is

$$U_d = \pi\sqrt{\frac{GJ}{\pi\rho_f e c^2 L^2}}, \tag{A.9}$$

which implies that $C_\phi = \pi$.

Appendix B

STRONG-FORM SOLUTION FOR CENTRIFUGAL BUCKLING IN A VACUUM

Starting from the strong form of the equation of motion for flexure and appending centrifugal effects yields the following expression previously shown in Equation (2.37)

$$\rho_s A\ddot{v} + EIv'''' - \rho_s A\Omega^2 v - \rho_s A\Omega^2 (x_\theta b)\phi = \rho_s A\Omega^2 R_0, \tag{B.1}$$

By considering the special case where there is no eccentricity between the E.A. and C.G. (i.e. $x_\theta = 0$) and assuming that $\ddot{v} = 0$ for the case of a static instability, Equation (B.1) can be reduced to

$$EIv'''' - \rho_s A\Omega^2 v = \rho_s A\Omega^2 R_0. \tag{B.2}$$

By defining a new term $\eta^4 = EI/\rho_s A\Omega^2$, Equation (B.2) can be rewritten as

$$\eta^4 v'''' - v = R_0. \tag{B.3}$$

The deformation field $v(x)$ can be solved explicitly using the following boundary conditions

$$v(0) = 0 \quad v(L) = 0$$

$$v'(0) = 0 \quad v'(L) = 0$$

which then yields

$$v(x) = R_0 \left(\frac{C_1(1 - C_2) + h(x)(C_2 - 1) + f(x)C_3(1 - g(x))(C_2 - g(x))}{C_1(C_2 - 1) + C_3(C_2 + 1)} \right), \tag{B.4}$$

where the terms C_1, C_2, and C_3 and the functions $f(x)$, $g(x)$, and $h(x)$ are defined as

$$C_1 = cos\left(\frac{L}{2\eta}\right) \quad C_2 = e^{L/\eta} \quad C_3 = sin\left(\frac{L}{2\eta}\right)$$
$$f(x) = e^{-x/\eta} \quad g(x) = e^{x/\eta} \quad h(x) = cos\left(\frac{L-2x}{2\eta}\right)$$

It can be seen from Equation (B.4) that the system will become unstable if either of the following conditions are met:

1. $\eta = 0$

2. $C_1(C_2 - 1) + C_3(C_2 + 1) = 0$

The first condition is met if the system has no flexure stiffness (i.e. $EI = 0$) and is therefore considered a trivial solution. The second condition is more difficult to assess because it represents a transcendental equation. By making the assumption that $C_2 - 1 \approx C_2 + 1$, an approximate solution can be obtained as

$$L/\eta \approx 2\pi\left(n - \frac{1}{4}\right) \qquad n = 1, 2, 3.... \tag{B.5}$$

Taking the first solution where $n = 1$ and checking the assumption of $C_2 - 1 \approx C_2 + 1$ reveals an error of about 1%. Continuing with $n = 1$ and substituting the definition of η back into Equation (B.5) then yields

$$\Omega_c \approx 22.2\sqrt{\frac{EI}{\rho_s A L^4}}, \tag{B.6}$$

where Ω_c is the turbine speed required to excite 1st mode centrifugal buckling.